SCIENTIFIC REPORTS

OPEN

Rapid confocal imaging of vesicle-to-sponge phase droplet transition in dilute dispersions of the $C_{10}E_3$ surfactant

Received: 17 October 2018
Accepted: 15 December 2018
Published online: 19 February 2019

André Pierre Schroder[1], Jérôme Joseph Crassous[2,3], Carlos Manuel Marques[1] & Ulf Olsson[3]

The lamellar-to-sponge phase transition of fluorescently labelled large unilamellar vesicles (LUVs) of the non-ionic surfactant triethylene glycol mono n-decyl ether ($C_{10}E_3$) was investigated *in situ* by confocal laser scanning microscopy (CLSM). Stable dispersions of micrometer-sized $C_{10}E_3$ LUVs were prepared at 20 °C and quickly heated at different temperatures close to the lamellar-to-sponge phase transition temperature. Phase transition of the strongly fluctuating individual vesicles into micrometre-sized sponge phase droplets was observed to occur via manyfold multilamellar morphologies with increasing membrane confinement through inter- and intra- lamellar fusion. The very low bending rigidity and lateral tension of the $C_{10}E_3$ bilayer were supported by quantitative image analysis of a stable fluctuating membrane using both flicker noise spectroscopy and spatial autocorrelation function.

The self-assembly of surfactants and lipids has been studied intensively for over a century[1–3], partly because of its important role in numerous applications[4], but also because of its direct relevance for bio-membranes[5] and for many biological processes[6]. Aqueous surfactant systems typically display a rich phase behavior with different liquid and liquid crystalline phases[7,8]. Phase equilibria depend on local intermolecular interactions in the surfactant monolayer, resulting in its spontaneous or preferred curvature, H_0, and on colloidal interactions between aggregates. Surfactant films were extensively modeled as flexible curved elastic surfaces for the investigation of microemulsions, bicontinuous cubic and sponge phases, lamellar phases and vesicles[9–12].

The monolayer curvature H_0 of non-ionic ethylene oxide based surfactants, C_iE_j ($CH_3(CH_2)_{i-1}(OCH_2CH_2)_jOH$), can be conveniently tuned by temperature making them very appealing model systems for the study of phase transitions[13,14]. Counting curvature away from water as positive, H_0 decreases with increasing temperature, approximately by 10^{-3} Å^{-1} K^{-1} for triethylene glycol mono n-decyl ether $C_{10}E_3$[13,14]. The low surfactant concentration part of the phase diagram of $C_{10}E_3$-water is shown in Fig. 1. Around $H_0 \approx 0$, bilayer structures are preferred and the binary phase diagram shows a lamellar phase (L_α) and a sponge phase (L_3), both of which coexisting with a dilute solution phase (W) at high dilution. In the $W + L_\alpha$ two phase region, the lamellar phase can often be fragmented into unilamellar vesicles[15]. The bending rigidity of the $C_{10}E_3$ bilayer was determined to be 5 k_BT at room temperature[16]. Vesicles, lamellar phase and sponge phase represent different topologies of the bilayer. Transitions between these states require bilayer fusion or fission, that can be triggered for such non-ionic system by temperature jump experiments. Kinetics of both L_α-to-L_3 and L_3-to-L_α phase transitions have been studied by time resolved NMR and small angle neutron scattering[17,18]. Fusion kinetics has also been studied by temperature jumps within the L_3 phase[19]. These studies concluded that membrane fusion requires essentially $H_0 < 0$ and that the rate of fusion increases with decreasing H_0. This picture was later confirmed by a vesicle stability study (Fig. 1)[15]. Extruded unilamellar vesicles, of average radius 25 nm, were found to be kinetically stable for temperatures below the three phase line $W + L_3 + L_\alpha$, while above this temperature the spontaneous fusion occurs with a rate that increases with increasing temperature. The three phase line temperature corresponds approximately to the temperature where H_0 changes sign[20,21].

This dependence of the fusion kinetics on H_0 is in agreement with previous experimental work on biological lipids and models of membrane fusion, involving a hemifusion stalk intermediate of negative monolayer

[1]Institut Charles Sadron, Université de Strasbourg, CNRS UP22, F-67200, Strasbourg, France. [2]Institute of Physical Chemistry, RWTH Aachen University, D-52074, Aachen, Germany. [3]Physical Chemistry, Department of Chemistry, Lund University, SE-22100, Lund, Sweden. André Pierre Schroder and Jérôme Joseph Crassous contributed equally. Correspondence and requests for materials should be addressed to A.P.S. (email: schroder@unistra.fr)

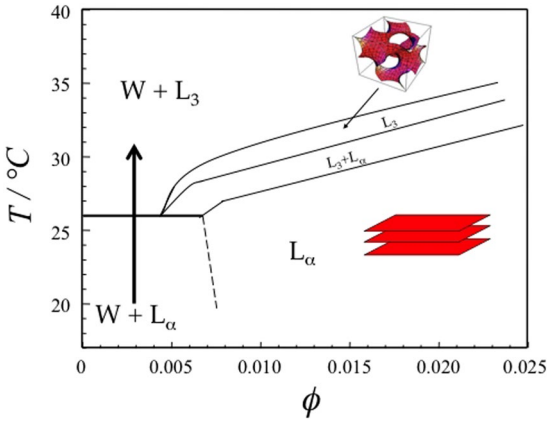

Figure 1. Partial phase diagram, at high water content, of the water-$C_{10}E_3$ system adapted from[15]. Here, L_α refers to lamellar phase, L_3 to a "sponge" (L_3) phase and W to a solution phase. ϕ denotes the surfactant concentration. The horizontal line at 26 °C corresponds to a three phase line, $W + L_\alpha + L_3$. The vertical arrow illustrates a typical temperature jump.

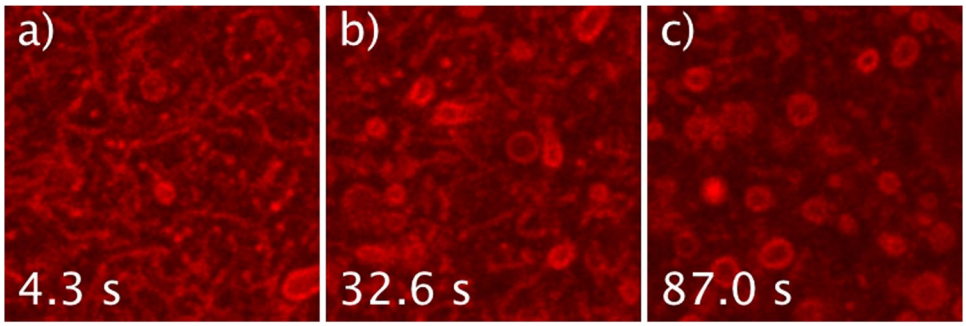

Figure 2. Typical evolution of a $C_{10}E_3$ solution that has experienced shearing during sample preparation. Images are taken from Supplementary Movie M2, during quenching at 30 °C. The solution is initially composed of tube-like structures, that evolve towards LUVs of average size of about 2 μm. The characteristic tube-to-LUV relaxation time decreases with T-quenching temperature. Similar shape relaxations also take place at room temperature, over ~30 min. Image width is 19.3 μm.

curvature[22–25]. Studies on lipid systems have shown that fusion kinetics depends on the membrane composition. Lipids having $H_0 > 0$, like single-chain oleoyl-lysophosphatidylcholine, prevent fusion, while lipids having $H_0 < 0$, like dioleoyl phosphatidylethanolamine promote membrane fusion.

If large enough vesicles can be prepared, they can be studied and characterized with optical microscopy[26,27]. In this paper we further characterize the fusion of vesicles and the topological transitions of $C_{10}E_3$ membranes with temperature. Using rapid laser scanning confocal microscopy, we follow how fluorescently labeled large unilamellar vesicles (LUVs) spontaneously fuse upon a temperature jump (hereafter named T-quenching, or quenching), following the vertical line in Fig. 1, *i.e.* crossing the horizontal separation line (horizontal three phase line $W + L_\alpha + L_3$) between the $W + L_\alpha$ and the $W + L_3$ regions. Final equilibrium structures vary from large multilamellar to droplet-like sponge phase objects depending on the quenching temperature. The sponge phase droplets formed here are analogous to the high genus vesicles studied by Noguchi[28,29] and may also serve as a model for certain cell organelles[30,31]. Furthermore, flicker noise spectroscopy and spatial autocorrelation were applied to analyze the shape fluctuations of an isolated $C_{10}E_3$ bilayer, allowing us to estimate the bilayer bending rigidity κ and the membrane internal tension σ_0.

Results

Imaging structural transformation. The vesicles are formed in the $W + L_\alpha$ two phase region where the vesicles are expected to coexist with $C_{10}E_3$ monomers (Fig. 1). The monomer solubility, *i.e.* critical aggregation concentration of $C_{10}E_3$ is $\phi_{CAC} \sim 2.10^{-4}$ at 25 °C[32], corresponding to ~5% of the overall surfactant.

At 20 °C the $C_{10}E_3$ dispersion contains mainly stable, large unilamelar vesicles (LUVs) of ~2–3 μm diameter (Fig. 2c and Supplementary Movie M1). That these LUVs exhibit high amplitude thermal fluctuations is consistent with (**i**) a reduced volume, $v = \frac{V}{4\pi R^3/3}$ smaller than one, V and R being the actual inner volume of the vesicle and the average radius of its apparent, equivalent sphere respectively, with (**ii**) a low bending rigidity of the $C_{10}E_3$ bilayer, *i.e.* $\kappa \simeq 5 k_B T$[16], and with (**iii**) a low enough value of the membrane lateral tension.

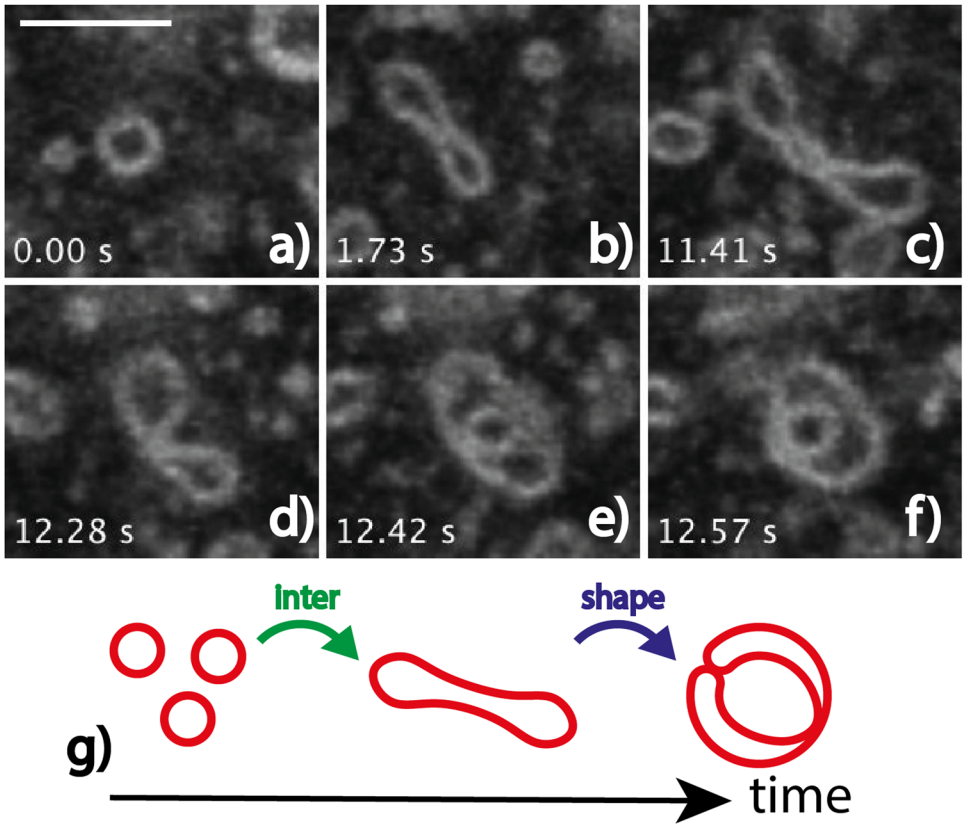

Figure 3. (**a**–**f**) Initial steps of multilamellar structure formation, here captured during T-quenching at 35 °C (image sequence extracted from Supplementary Movie M3). Similar evolutions of initial LUVs were observed during any T-quenching experiment (28, 30, and 35 °C, see Supplementary Movies M4–M8). (**g**) Scheme of the shape evolution with time: 'inter' is for inter-object fusion, and 'shape' for change-of-curvature-induced shape change. Time t = 0 s is arbitrary chosen. Scale bar is 5 μm.

When quenched at 28, 30, or 35 °C, LUVs undergo shape and structure transformations that we describe in the following. T-quenching experiments were repeated 3 to 5 times, Figs 2, 3, 4, 5 and 6 retain some of the typical structures observed during these experiments. When tubular vesicles induced by shearing during sample preparation (Methods section) are present in the initial dispersion, they systematically evolve towards LUVs (Fig. 2) prior to any other kind of membrane shape evolution. Such process takes several tens of seconds to a few minutes, depending on the quenching temperature, but it also takes place at 20 °C, over a longer time, *i.e.* ~30 min.

Figure 3 shows a typical transformation under T-quenching, of an initial, at equilibrium LUV, a process that takes ten to twenty seconds. A unilamellar vesicle first grows in size while elongating (Fig. 3b,c), and then curves until closure (Fig. 3d–f), forming a 'bilamellar' structure. Images in Fig. 3, extracted from Supplementary Movie M3, correspond to optical z-cuts taken at a fixed z-position in the sample. Movies of such vesicle evolution were also acquired while cycling over the z-position, refered to as (z, t) scans, see Supplementary Movie M4 that is a 3D averaging projection of such scan. They strongly suggest that the intermediate, elongated structures similar to those in Fig. 3b–d have a biconcave disk shape, while the final object in Fig. 3f, exhibits average spherical symmetry (Supplementary Movie M4). Insets in Fig. 4b (T-quenching 28 °C) further confirm this assumption. Thus, the most likely scenario for the initial LUV transformation upon T-quenching consists of a growth towards a "red blood-cell"-like structure followed by an invagination, leading to an onion-like object (Fig. 3g). We attribute the process of membrane area growing in Fig. 3b,c to membrane fusion, referred to as 'inter' (-object fusion) in Figs 3, 4 and 5. Indeed, our observations exclude a significant contribution of a membrane-enrichment process via the solubilized fraction of the $C_{10}E_3$ molecules, that would require a simultaneous decrease in size of neighboring LUVs in the sample similarly to the Ostwald ripening process[33], a phenomenon never observed in our experiments (see Supplementary Movies M4–M8). Fusion events of small LUVs could not be resolved, we could however catch some fusion events of multilamellar objects. Besides, the shape evolutions shown in Figs 3c–e, 4 and 5, corresponding to the 'shape' transition schematically depicted in the figures, is compatible with the expected tendency of the $C_{10}E_3$ bilayers to form saddle shape structures (invagination process) while temperature increases in the sample, to accommodate for the concomitant decrease in H_0. Objects similar to Fig. 3f were seen to only persist over short times (several seconds), before undergoing further structural transformations, leading to either larger and topologically more complex multilamellar objects, or denser L_3 phase droplets.

When quenched at 28 °C, the initial unilamellar vesicles mainly transform into larger multilamellar L_α structures through repeated sequences of growth, anisotropic deformation, fusion, invagination, leading to objects

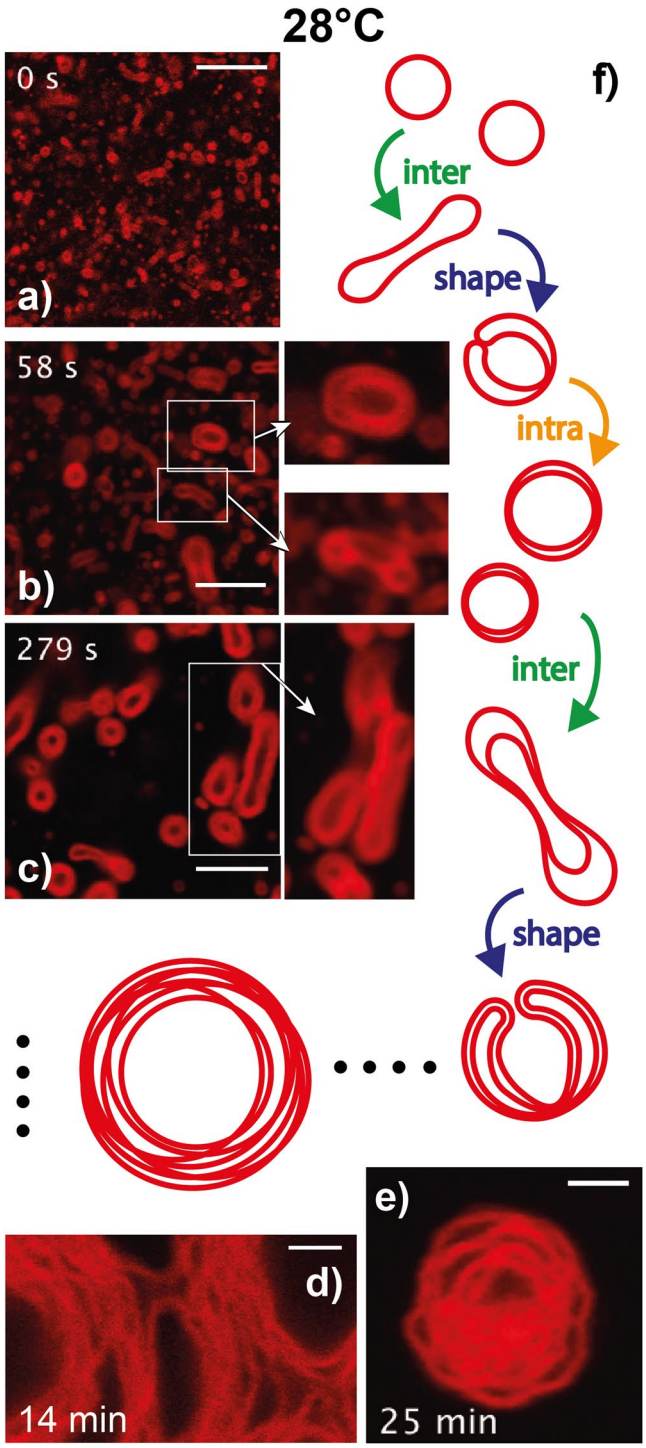

Figure 4. Membrane structures captured during T-quenching at 28 °C. (**a**–**c**) Evolution of initial LUVs into (apparently) bilamellar or trilamellar structures. (**d**–**e**) Equilibrated multilamellar, onion-like structures, exhibiting no or very slow structure evolution. (**f**) The self-assembly process and structural evolution are schematically depicted in steps, including 'inter'-particle fusion, 'shape' transformation, and 'intra'-particle fusion. Scale bars are 10 μm in (**a**–**c**) and 2 μm in (**d**,**e**).

often presenting more than ten apparent membrane layers. Stable structures were obtained after 3 to 8 min, keeping in mind that stability is considered over an experimental time scale of ~30 min. Typical stable multilamellar structures are shown in Fig. 4d,e, being whether onion-like, *i.e.* symmetric (Fig. 4e), or non symmetric (Fig. 4d), as shown in Supplementary Movies M9–M11. On the contrary, T-quenching at 30 °C (resp. 35 °C) results after a period of 2 to 5 (resp. 0.5 to 3) min in dispersions containing mainly L_3 droplets capable of fusion

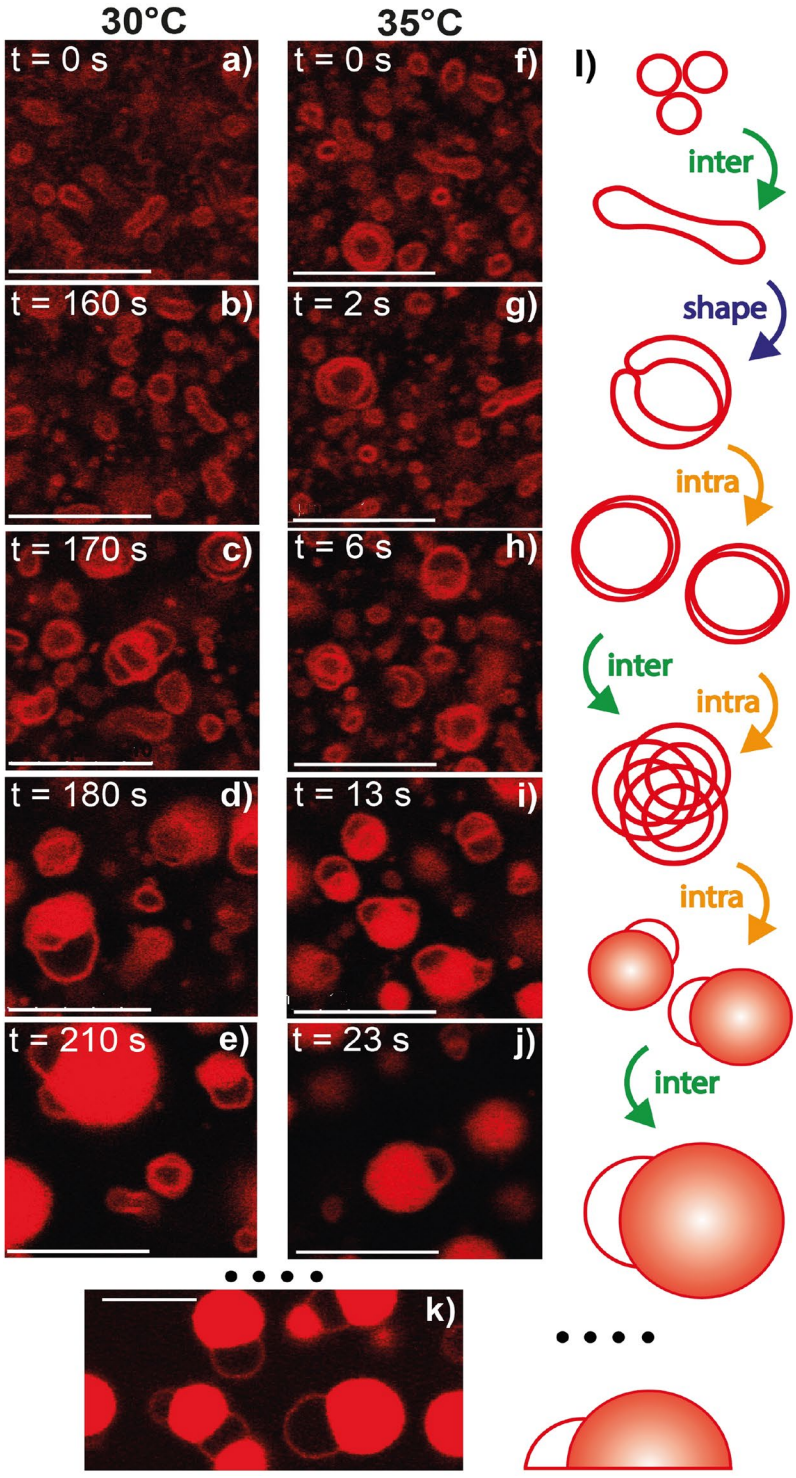

Figure 5. Structures captured during T-quenching at 30 and 35 °C. (**a**,**f**) Initial vesicles. (**b**–**e**,**g**–**j**) Transient bilayer structures described in Fig. 3 and their further evolution towards final, droplet-like, L_3 structures. (**k**) L_3 droplets adsorbed on the bottom glass surface, observed several minutes after their formation. (**l**) The schematics depicts probable steps of structure evolution, with a strong competition of 'intra'- and 'inter'-particle fusion, leading to ~μm-sized L_3 droplets (see Supplementary Movies M6 and M8). Scale bars are 10 μm.

with neighboring analogs upon contact (Fig. 5e,j, Supplementary Movies M6, M12 and M13), which eventually adsorb at the bottom coverslip of the observation chamber in less than 2 min (Fig. 5k).

Morphological transitions of the bilayers during the quenching experiments are sketched in Fig. 4f (28 °C) and in Fig. 5l (30 and 35 °C). Beside 'inter'-object fusion and 'shape' transition (Fig. 3) was an 'intra'-object

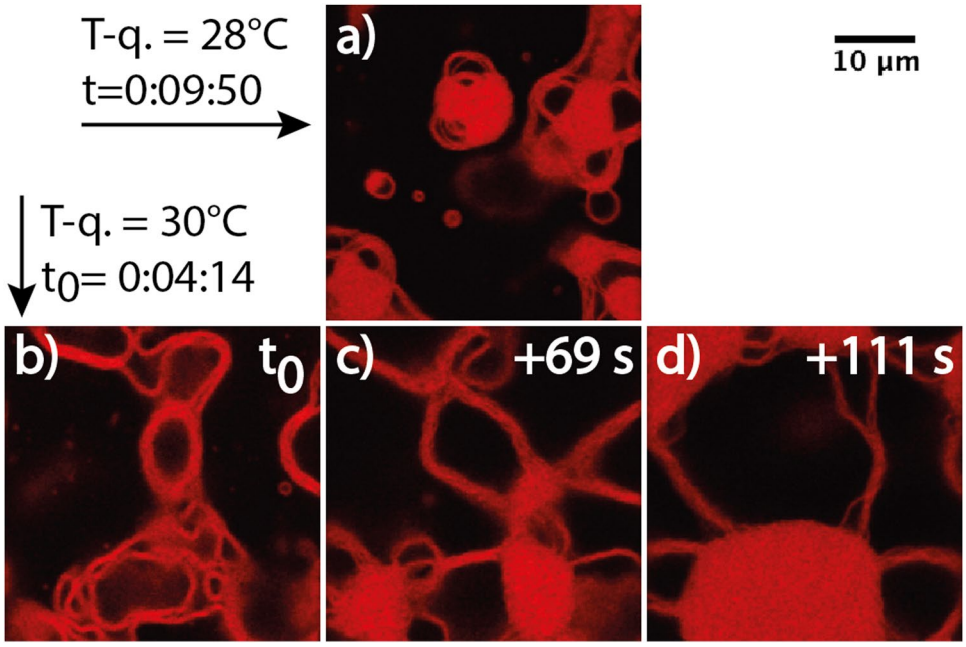

Figure 6. Rare objects found at 28 °C (**a**) and 30 °C (**b**–**d**). While objects in (**a**) are stable over minutes (Supplementary Movie M14), objects in the sequence (**b**–**d**) have been captured during a continuous fusion process, ending into optically dense droplets of multiply connected bilayers, as in the macroscopic L_3 phase (Supplementary Movie M12).

fusion process clearly evidenced upon T-quenching experiments at 30 and 35 °C, while to a less extent upon T-quenching at 28 °C (Figs 4f and 5l respectively). Schematically we can describe the overall process after a temperature jump as follows. It begins with the fusion of the initial unilamellar vesicles. Such events, when they occur, are rapid and not resolved in our experiments for initial LUVs. However, we clearly see the decrease in the number density of vesicles and the increase of their average size. From these very first moments is the local temperature increase of the sample related to a decrease of H_0, and hence to a bilayer topology transformation resulting in a gradual decrease of the average Gaussian curvature, $\langle K \rangle$, and the Euler characteristic, $\chi_E = \langle K \rangle A_b / 2\pi$[34], of the membrane, where A_b is the bilayer membrane area. Bilayers accommodate that temperature increase with the creation of saddle points, that in turn results in the 'shape' transformation depicted above, *i.e.* in the evolution towards onion-like structures with an increased number of bilayers. As seen in Fig. 3 and in Supplementary Movies M3–M8, such 'shape' transformation process expands over several seconds. For a low enough temperature increase, and certainly for a low enough value of the rate of temperature increase has the system the time to evolve through the building of such multilamellar objects, where bilayers still exhibit micrometer range values of their radius of curvature. This corresponds mainly to 28 °C T-quenching experiments (Fig. 4b–e). Besides, is the rate of local temperature increase much higher upon T-quenching at 30 °C and 35 °C, concomitant to a stronger and faster decrease of H_0. As a consequence, bilayers certainly cannot undergo the required rate of sequences of 'inter'-fusion and 'shape'-transformation in order to accommodate with the corresponding high number of saddle points. The system thus rearranges through 'intra'-fusion processes, leading to a denser organisation of the bilayers, with sub-micron range values of their local radius of curvature. This gradual topology transformation and increase of the bilayer volume fraction, ϕ of the structures, is expected to terminate when ϕ reaches the value at the sponge phase binodal line to the given temperature. From the phase diagram, we thus expect the steady state ϕ in the sponge phase droplets to increase with increasing temperature. Our experiments show that a wide variety of structures coexist during T-quenching. As a matter of fact, it can be considered that a competition between inter-vesicle and intra-vesicle fusion is taking place, controlled by the local rate of temperature increase. Thus, that variety of structures found is likely the result of that competition. An example of such variety is given in Fig. 6. One the one side, at 28 °C, amongst major onion-like structures, were found some rare, denser structures that did not fuse at the experimental time scale (Fig. 6a, Supplementary Movie M14), while at 30 °C, amongst major L_3 droplets, were found big, space extended structures, similar to the ones shown in Fig. 6a, but with a strong fusogenic character (Fig. 6b–d, Supplementary Movie M12).

We note that the sponge phase droplets often contain one or more unilamellar membrane "domes", as seen in Fig. 5e,j. Certainly, dome precursors are seen in Fig. 6a and Supplementary Movies M14 and M15. While in those, stable intermediary structures (28 °C), multiple bilayers are observed, this is rarely the case in L_3-phase droplets, *i.e.* at 30 and 35 °C (Fig. 5e,j), where most often only one dome remains per droplet. Similar domes are also often observed on cubosomes[35], that could be seen as the crystalline analogs of sponge phase droplets. In the bicontinuous cubic phase the multiply connected bilayer has crystallized in a cubic lattice, while being disordered (liquid) in the case of the sponge phase. In both cases however, the multiply connected bilayer has to meet droplet interface in a particular way to avoid unfavorable bilayer edges. Confined between two solid surfaces, a sponge phase was found

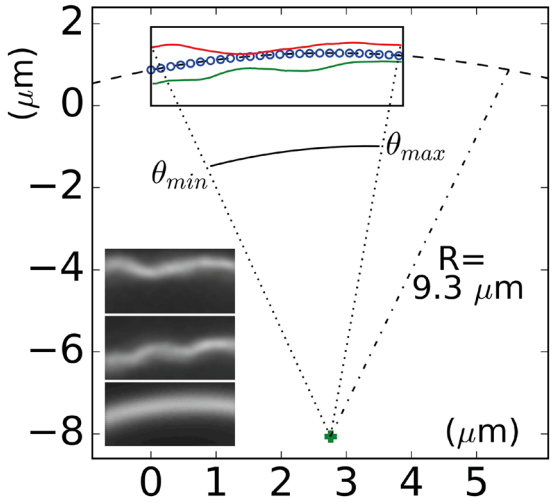

Figure 7. Insets from top to bottom, two snapshots of Supplementary Movie M16, and average image over the whole movie. Rectangle is the movie window (128×64 pixel$^2 = 3.87 \times 1.92\,\mu$m^2), that contains the calculated fluorescence maximum profiles of the three fluorescence images given as insets (see SI section for the detailed procedure of profile extraction). Dotted line is the average intensity profile best fit with a circle of radius 9.3 μm, green cross is the calculated center of symmetry of the circular best fit.

Bending modulus (k_BT units)	literature[16]	spectrum analysis	autocorrelation analysis
κ	4.95 ± 0.2	1.7	3.9

Table 1. Bending modulus κ as calculated from spectrum analysis and autocorrelation analysis, and comparison with measured data from literature.

to form planar lamellae[36]. Hereby, the sponge phase droplets are pictured as having a unilamellar bilayer envelope, from which the multiply connected sponge structure grows inward as it necks in the envelope. Surprisingly, those domes remain present once L_3-phase droplets have adhered on the bottom glass substrate (Fig. 5k).

Bending modulus of a single bilayer. Mechanical properties of fluid membranes have been extensively studied over the last three decades starting with the pioneering work by Helfrich[9,37–39]. This field of research was born with the growing interest in phospholipid bilayers, that not only appeared as model systems of cell membranes, but also as interesting tools for investigating soft matter physics. Thanks to their very low solubility, typically in the order of pM to nM, phospholipids build, indeed an almost perfect system, *i.e.* free standing bilayers in a surfactant-free solution. Conversely, $C_{10}E_3$ has a non negligible monomer solubility, representing 5% of the molecules in our experiments. However, this work demonstrates that $C_{10}E_3$ membranes exhibit long term stability at a constant temperature, *i.e.* over tens of minutes, though continuously exchanging surfactant molecules with their aqueous environment.

We imaged a fluctuating bilayer at a frame rate of 172 frames/sec, that was found to be sufficiently high to enable the resolution of the membrane fluctuations (see Supplementary Movie M16, and Fig. 7). The imaged membrane corresponded to a region of a dome from a stable multilamellar structure at 28 °C, similar to the one shown in Supplementary Movie M15. The observed section of membrane was distant enough from the rest of the structures so that no steric interactions with another membrane was observed during the movie. Images were processed as described in the SI section, in order to extract the membrane profile $(x(t), y(t))$ with sub-micron resolution. Figure 7 shows two typical snapshots of the Supplementary Movie M16 together with the time averaged image of the movie (grey level insets, average on bottom), as well as the corresponding extracted profiles (rectangular window). As seen in the figure, the average membrane profile is circular, with a radius of curvature $R = 9.3 \pm 0.1\,\mu$m, thus showing that domes are sections of a sphere. $(x(t), y(t))$ profiles were further converted into circular coordinates, and expressed in terms of $r(\theta(t), t)$, the radius of the profile from the center of symmetry of the spherical dome, $\theta(t)$ being the angle variable in the cylindrical reference space (in 2D geometry in the images). Finally, we calculated the height function $h(\theta, t)$ between average and instantaneous membrane profiles as described in the SI section.

Following methods well described in literature, we applied flicker noise spectroscopy to the space or time variations of the $h(\theta, t)$ curves, to extract the bending rigidity κ of the membrane: Table 1 compares κ obtained from the analysis of the average fluctuation spectrum[40] and from the evaluation of the average angular autocorrelation function[41] of the membrane profile. Both values are close to the value published in literature[16]. Detailed calculations for κ are given in SI section.

Discussion

Our study demonstrates the applicability of rapid confocal microscopy and highly fluctuating $C_{10}E_3$ vesicles to investigate complex membrane fusion processes *in situ* through T-quenching. Those assembly processes are driven by the L_α-to-L_3 phase transition of the surfactant, being characterized by the inter and intra fusion of suspended unilamellar vesicles (LUVs), and the formation of either large multilamellar objects or micrometric sponge phase droplets. This was made possible first, by working with dilute samples (0.003 w/w), and secondly, by quenching samples initially in the L_α phase at three temperatures close to and above the L_α-to-L_3 transition temperature. For the lowest temperature quenching, *i.e.* 28 °C, we describe how primary LUVs evolve over minutes towards multilamellar objects with increasing number of membranes and local membrane concentration. We also show more rare metastable structures, that appear as intermediates between the lamellar phase L_α and the L_3 sponge phase, being characterized by such an increased local surfactant density that no more individual membranes can be seen with our optical technique. In comparison, temperature quenching at 30 °C or 35 °C led to much faster kinetics of membrane transformation. As a consequence, most of the intermediate structures seen at 28 °C were never observed, and LUVs were evolving over a few seconds towards the sponge phase droplets. Finally, we could record an isolated fluctuating part of a membrane at 28 °C, that we analyzed using both flicker noise spectroscopy, and spatial autocorrelation, to estimate the bending modulus κ of the membrane at that temperature. Our measurement of the bending modulus provides values in the range of 2–4 k_BT, in good agreement with literature values[16].

Methods

Vesicle solution and sample preparations. $C_{10}E_3$ (Sigma Aldrich) was mixed with an amphiphilic dye (BODIPY® 558/568-C12, from Life Technologies) at a dye/$C_{10}E_3$ fraction of 0.3 mol%. This mixture was diluted at a mass concentration 3.33 g/L in 18 MΩ deionized water (Merck Millipore, Germany), corresponding to a molar concentration 11.5 mM, and to a volume fraction $\phi = 0.315\%$, considering a density $\rho = 0.94\,g/cm^3$ [32]. Once prepared, the dispersion was gently shaked during three minutes. Such solution showed long term stability at 20 °C, as observed under the microscope. The stock solution was used within 2 days. Observation cells were build using the following protocol: a 1 mm thick double face tape, with a 6 mm diameter pinched hole was stuck on one side of a glass coverslip, forming a cuvette, in which 28 μL of the vesicle solution was injected. The well was then closed by sticking on the free tape side a 1 mm thick glass slide, resulting in a watertight observation cell. The preparation was done at room temperature, *i.e.* at 20 ± 1 °C. It is worth noting that $C_{10}E_3$ vesicles are shear sensitive. The transfer of the 28 μL droplet was done using a pipette tip (Eppendorf, Germany); the sample injection eventually resulted in the shearing of the vesicles into long membrane tubes that relaxe over tens of minutes at 20 °C, and over less than five min during one typical T-quenching experiment, with a strong dependence on both jump temperature and sample preparation conditions. Such evolution is shown in Supplementary Movie M2 and Fig. 2a–c.

Confocal microscopy. The confocal micrographs were recorded on a Leica SP5 CLSM (Germany) operated in the inverted mode (D6000I) using a 100×, 1.4 NA, oil-immersion objective. A 543 nm He-Ne laser was used to excite the amphiphilic dye. The samples were monitored *in situ* at different temperatures, and an environmental system was used to ensure temperature control with an accuracy of 0.2 °C. The microscope was equilibrated over one hour at the quenching temperature before starting the experiments. A typical T-quenching experiment ran as follows: an observation chamber filled with the LUVs was placed on the microscope stage just after it has been sealed, and the real time confocal imaging was started as soon as possible; we consider that image recording started within less than 1 min (typically 30 s) after the observation cell was placed in the microscope. For each T-quenching experiment the first image sequence was acquired at a frame rate ~10 to 30 frames/s, during 1 to 5 min, in a region of the sample located ~50 μm above the coverslip. Then, other image sequences were acquired at different positions in the sample, with the purpose of collecting images on all possible structures present in the dispersion. In particular, reducing the field of view while increasing the frame rate (up to ~200 frames/s) enabled, at high magnification and resolution, to resolve the membrane thermal fluctuations.

Confocal images of lamellar and sponge phase structures are shown without modification except global image contrast enhancement and smoothing if necessary.

References

1. McBain, J. W. & Taylor, M. K. Über die elektrische leitfähigkeit von seifenlösungen. *Berichte* 321–322 (1910).
2. Hartley, G. S. *Aqueous Solutions of Paraffin Chain Salts*. (Hermann et Cie, Paris, 1936).
3. Winsor, P. A. *Solvent Properties of Amphiphilic Compounds*. (Butterworth Scientific Publ. Ltd., London, 1954).
4. Holmberg, K. *Handbook of Applied Surface and Colloid Chemistry*. (John Wiley & Sons Ltd., Chichester UK, 2002).
5. Epand, R. *Lipid Polymorphism and Membrane Properties*. (Academic Press, San Diego USA, 1997).
6. Lipowsky, R. & Sackmann, E. *Structure and Dynamics of Membranes*. (Elsevier Science B.V., Amsterdam, 1995).
7. Laughlin, R. G. *The Aqueous Phase Behavior of Surfactants*. (Academic Press, San Diego USA, 1994).
8. Kronberg, B., Holmberg, K. & Lindman, B. *The Aqueous Phase Behavior of Surfactants*. (Wiley, Chichester UK, 2014).
9. Helfrich, W. Elastic properties of lipid bilayers - theory and possible experiments. *Z. Naturforsch.* **28c**, 693–703 (1973).
10. Safran, S. A. *Statistical Thermodynamics of Surfaces, Interfaces and Membranes*. (Addison-Wesley, Reading MA, USA, 1994).
11. Wennerström, H. & Olsson, U. Microemulsions as model systems. *C. R. Chemie* **12**, 4–17 (2009).
12. Porte, G., Appell, J., Bassereau, P. & Marignan, L. Microemulsions as model systems. *J. Phys. (Paris)* **50**, 4243 (1989).
13. Olsson, U. & Wennerström, H. Globular and bicontinuous phases of nonionic surfactant films. *Advances in Colloid and Interface Science* **49**, 113–146 (1994).
14. Strey, R. Microemulsion microstructure and interfacial curvature. *Colloid and Polymer Science* **272**, 1005–1019 (1994).
15. Bulut, S., Zackrisson Oskolkova, M., Schweins, R., Wennerström, H. & Olsson, U. Fusion of nonionic vesicles. *Langmuir* **26**, 5421–5427 (2010).
16. Bulut, S., Åslund, I., Topgaard, D., Wennerström, H. & Olsson, U. Lamellar phase separation in a centrifugal field. A method for measuring interbilayer forces. *Soft Matter* **6**, 4520–4527 (2010).

17. Gotter, M., Strey, R., Olsson, U. & Wennerström, H. Fusion and fission of fluid amphiphilic bilayers. *Faraday Discussions* **129**, 327–338 (2005).
18. Gotter, M. *et al*. A comprehensive, time-resolved sans investigation of temperature-change-induced sponge-to-lamellar and lamellar-to-sponge phase transformations in comparison with ^{2}H-NMR results. *European Physical Journal E* **24**, 277–295 (2007).
19. Le, T. D. *et al*. Relaxation kinetics of an L_3(sponge) phase. *Journal of Physical Chemistry B* **106**, 9410–9417 (2002).
20. Anderson, D., Wennerström, H. & Olsson, U. Isotropic bicontinuous solutions in surfactant-solvent systems: the L_3 phase. *Journal of Physical Chemistry* **93**, 4243–4253 (1989).
21. Le, T. D., Olsson, U., Wennerström, H. & Schurtenberger, P. Thermodynamics of a nonionic sponge phase. *Physical Review E* **60**, 4300–4309 (1999).
22. Siegel, D. P. Energetics of intermediates in membrane fusion: Comparison of stalk and inverted micellar intermediate mechanisms. *Biophysical Journal* **65**, 2124–2140 (1993).
23. Kozlovsky, Y. & Kozlov, M. M. Energetics of intermediates in membrane fusion: Comparison of stalk and inverted micellar intermediate mechanisms. *Biophysical Journal* **82**, 882–895 (2002).
24. Chernomordik, L. V. & Kozlov, M. M. Protein-lipid interplay in fusion and fission of biological membranes. *Annual Review of Biochemistry* **72**, 175–207 (2003).
25. Chernomordik, L. V. & Kozlov, M. M. Mechanics of membrane fusion. *Nature Structural & Molecular Biology* **15**, 675–683 (2008).
26. Bivas, I., Hanusse, P., Bothorel, P., Lalanne, J. & Aguerre-Chariol, O. An application of the optical microscopy to the determination of the curvature elastic modulus of biological and model membranes. *Journal de Physique (France)* **48**, 855–867 (1987).
27. Faucon, J. F., Mitov, M. D., Meleard, P., Bivas, I. & Bothorel, P. Bending elasticity and thermal fluctuations of lipid membranes. Theoretical and experimental requirements. *Journal de Physique (France)* **50**, 2389–2414 (1989).
28. Noguchi, H. Shape transitions of high-genus fluid vesicles. *Europhysics Letters* **112**, 58004 (2015).
29. Noguchi, H. Construction of nuclear envelope shape by a high-genus vesicle with pore-size constraint. *Biophysical Journal* **111**, 824–831 (2016).
30. Mannella, C. A. Structure and dynamics of the mitochondrial inner membrane cristae. *Biochim. Biophys. Acta - Molecular Cell Research* **1763**, 542–548 (2006).
31. Westrate, L. M., Lee, J. E., Prinz, W. A. & Voeltz, G. K. Form follows function: the importance of endoplasmic reticulum shape. *Annual Review of Biochemistry* **84**, 791–811 (2015).
32. Guégan, R. Intercalation of a Nonionic Surfactant (C10E3) Bilayer into a Na-Montmorillonite Clay. *Langmuir* **26**, 19175–19180 (2010).
33. Weiss, J., Canceliere, C. & J, M. D. Mass transport phenomena in oil-in-water emulsions containing surfactant micelles: Ostwald ripening. *Langmuir* **16**, 6833–6838 (2000).
34. Pressley, A. *Elementary Differential Geometry*. 2nd ed., (Springer Verlag, London, 2010).
35. Barauskas, J., Johnsson, M., Joabsson, F. & Tiberg, F. Cubic phase nanoparticles (cubosome): Principles for controlling size, structure, and stability. *Langmuir* **21**, 2569–2577 (2005).
36. Petrov, P., Miklavcic, S., Olsson, U. & Wennerström, H. A confined complex liquid. oscillatory forces and lamellae formation from an l3 phase. *Langmuir* **11**, 3928–3936 (1995).
37. Helfrich, W. Steric Interaction of Fluid Membranes in Multilayer Systems. *Z. Naturforsch. A* **33**, 305–315 (1978).
38. Servuss, R. M., Harbich, W. & Helfrich, W. Measurement of Curvature-Elastic Modulus of Egg Lecithin Bilayers. *Biochim. Biophys. Acta* **436**, 900–903 (1976).
39. Seifert, U. Configurations of fluid membranes and vesicles. *Advances In Physics* **46**, 13–137 (1997).
40. Pécréaux, J., Döbereiner, H.-G., Prost, J., Joanny, J.-F. & Bassereau, P. Refined contour analysis of giant unilamellar vesicles. *The European Physical Journal E* **13**, 277–290 (2004).
41. Drabik, D., Przybylo, M., Chodaczek, G., Iglič, A. & Langner, M. The modified fluorescence based vesicle fluctuation spectroscopy technique for determination of lipid bilayer bending properties. *Biochim. Biophys. Acta – Biomembranes* **1858**, 244–252 (2016).

Acknowledgements

The authors acknowledge financial support from the European Commission under the Seventh Framework Program by means of the grant agreement for the Integrated Infrastructure Initiative N. 262348 European Soft Matter Infrastructure (ESMI). Authors also aknowledge Ambassade de France, Institut Français de Suède, for supporting the project. U.O. and J.J.C. thank the Knut and Alice Wallenberg Foundation (project grant: KAW 2014.0052) for financial support.

Author Contributions

A.P.S., J.J.C., C.M.M. and U.O. conceived the experiments, A.P.S. and J.J.C. conducted the experiments and analyzed the results. A.P.S., J.J.C., C.M.M. and U.O. reviewed the manuscript.

Additional Information

Supplementary information accompanies this paper at https://doi.org/10.1038/s41598-019-38620-9.

Competing Interests: The authors declare no competing interests.

Publisher's note: Springer Nature remains neutral with regard to jurisdictional claims in published maps and institutional affiliations.

Rapid confocal imaging of vesicle-to-sponge phase droplet transition in dilute dispersions of the $C_{10}E_3$ surfactant.

André Pierre Schroder, Jérôme Joseph Crassous, Carlos Manuel Marques, and Ulf Olsson

1 SUPPLEMENTARY INFORMATION

1.1 Maximum fluorescence profile determination

An 'isolated' region of a connected membrane was imaged with the confocal fluorescence microscope at a rate of 172 frames per second, with the constraint that the membrane never moved out of the observation field, and always joined the two vertical borders of the image (SI.Fig. 1a, Movie ESI.M16). Window size in Movie ESI.M16 corresponds to 128×64 pixel^2, *i.e.* 3.87×1.92 μm^2. We extracted from the movie a continuous sequence of 1276 images, corresponding to ∼7.4 seconds, that we used for the analysis described below. Thanks to these (small) dimensions and (fast) acquisition frame rate, image bluring that induces a lack of precision in the membrane profile localization was minimized. We established a protocol to extract the main intensity profile of the membrane in each image, that we describe now. Similar protocols have been published in the case of round shaped profiles of GUVs, whether with phase contrast[?] or fluorescence microscopy[?] imaging.

SI.Fig. 1a is a snapshot of Movie ESI.M16. Each original image was first completed with a frame of 16 pixels width (new image size = 160×96 pixel^2), with grey values choosen as follows : upper and lower bands (16 pixels height each) were filled with a unique grey level, equal to the average grey of the first and last row of the original image. Each row of the original image was completed on its left and right side by 16 pixels with a value equal to that of the corresponding border pixel (SI.Fig 1b). The image was then smoothed by replacing each pixel value $I_{x',y'}$ by the value $I_{x,y}$ given by

$$I^{(L)}_{x,y} = \frac{\sum_{x',y'} I_{x',y'} \exp\left[-\frac{(x'-x)^2+(y'-y)^2}{L^2}\right]}{\sum_{x',y'} \exp\left[-\frac{(x'-x)^2+(y'-y)^2}{L^2}\right]}$$

with x,y (and x',y') the column and raw indices of the image. x',y' were choosen such that $\sqrt{(x'-x)^2+(y'-y)^2} < L$ (SI.Fig. 1c). The value $L = 4$ was the smallest value that blurred the image such that fluorescence intensity along each column of the image exibits a smooth pic shape, and also such that the full collection of these fluorescence maxima along the image width composes a continuous curve, as shown in SI.Fig. 1d. At this stage a first estimation of the membrane profile is therefore a collection of 128 maxima $M_{i(i=0..127)} = (i, y_i^M)$, with integer coordinates (SI.Fig 1g, empty squares). The following procedure applied to each M_i reads to sub-pixel resolution: five, 21 pixels long, intensity lines centered on M_i, along i) the vertical (Oy) direction ($\phi = 0$), and along ii) the directions oriented with angles $\phi = 22.5°, 45°, -22.5°, -45°$ with respect to the (Oy) axis, were extracted, as shown in SI.Fig. 1e,f. Each of the five intensity data sets were then fitted with a quadratic function, $I_i^\phi = a_i^\phi * dl_\phi^2$, dl_ϕ being the displacement variable along the ϕ direction (SI.Fig. 1f). The maximum of each fitting line was then converted into subpixel, *i.e.* real number coordinates $(x^M_{i,\phi}, y^M_{i,\phi})$. Not each of the five coordinates had how-

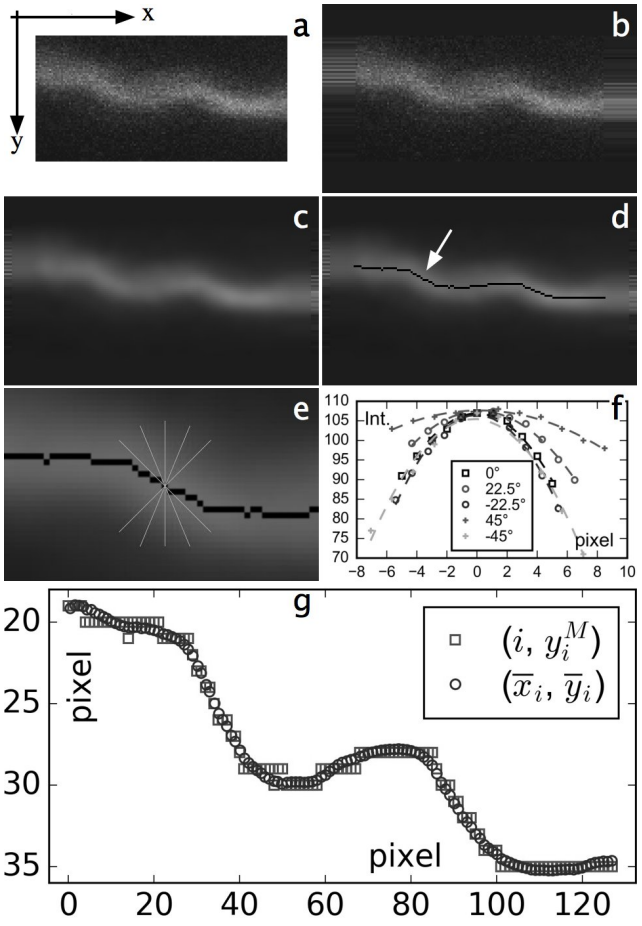

Fig. 1 : a) Snapshot of Movie ESI.M16. An isolated, but still connected to a bigger multilamellar structure (image not shown), membrane is captured at a frame rate of 172 frames/sec; b) original image is extended with a frame of width 16 pixels; c) smoothing of b) as described in the text; d) maximum intensity profile of the membrane, as obtained by highlighting the highest intensity pixels in each pixel column; e) zoom of d) arround the white arrow in d) and scheme of the 5 lines over which the fluorescence intensity is extracted and analyzed; f) the five intensity lines for the five lines in e), 0° corresponds to the vertical direction, white pixel would take the value 255; g) pixel (□) and sub-pixel (○) resolution maximum fluorescence intensity profiles for the whole membrane shown in a).

ever the same level of confidence. Indeed one expects that intensity profiles with a direction closer to the local membrane profile orientation are less trustable than intensity lines that are close to the normal to the local membrane profile. For each M_i, profiles with 'poor' orientation were determined as the ones with a second order coefficient of their quadratic fit intensity profile a_i^ϕ more than two times smaller than the highest quadratic coefficient of the set of five ϕ directions; they were ignored in the following of the procedure. Then, the center of mass $(\bar{x}_i, \bar{y}_i)$ of the remaining maxima was calculated for each M_i, by weighting each maximum position $(x^M_{i,\phi}, y^M_{i,\phi})$ with the quadratic value a_i^ϕ of the corresponding intensity line. The final maximum intensity profile of the membrane is thus a new collection of 128 points with sub-pixel precision, a fortiori not equally spaced in the (Ox) direction. SI.Fig. 1g shows the intensity profile (i, y_i^M) (pixel resolution) and the final sub-pixel profile $(\bar{x}_i, \bar{y}_i)$ for image SI.Fig. 1a. In the following, $(\bar{x}_i, \bar{y}_i)$ profiles will be refered to as $(x_i(t), y_i(t))$, with t the time variable, corresponding equivalently to the image index, or even simply, by $(x(t), y(t))$, with the implicit decomposition of the profile into 128 discrete values, fixed by the geometry of Movie ESI.M16.

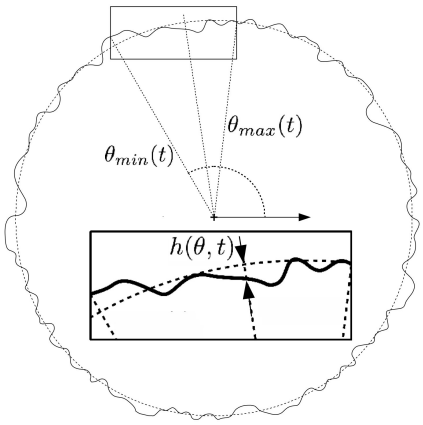

Fig. 2 : Scheme of an equatorial section of a spherical membrane, at time t. The membrane profile, originally expressed as a set of $(x(t), y(t))$ coordinates (pixels or subpixels), can be expressed into a cylindrical $(\theta, r(\theta,t))$ representation. $h(\theta,t)$ is the distance function between the membrane and it's average, round shape position (dotted curve). In the present case, due to the restricted area of observation, the instantaneous $(\theta_{min}(t), \theta_{max}(t))$ limits do not corresond to the $(\theta_{min}, \theta_{max})$ limits choosen for the analysis of the whole movie (see the text).

Flicker noise spectroscopy of membranes is most frequently applied through the shape analysis of the 2D projection of 3D vesicles.[???] Averaging Movie ESI.M16 has shown that the studied membrane has here an average circular shape (Fig. 7 in main article). We thus argue that we can use a similar protocol to that reported in litterature, under suitable precautions. SI.Fig. 2 shows the equator section of a membrane with an average spherical shape. The 2D-projected membrane fluctuates overtime around it's average, circular shape due to thermal energy, with an amplitude spectrum that depends on both its bending modulus κ and its internal tension σ.[?] Following the litterature, original $(x(t), y(t))$ membrane profiles are better analyzed under the form of $r(\theta,t)$ profiles, *i.e.* the distance function between the membrane and the center of the vesicle. Implied in this cartesian to cylindrical transformation is a decomposition of the contour into a set of θ angle values regularly spaced in the $[0..2\pi]$ range, common to all images,[??] as far as a closed, almost circular contour is studied. However a partial, opened contour can be studied as well, as described elsewhere.[?] Let's assume one captures one region of such 2D projection, *i.e.* in a rectangular window as schematized in SI.Fig. 2. Applied to our experiment, the center of the circular best fit to the average profile (see above) has to be chosen as the center of symmetry for the cartesian to cylindrical variable conversion (Fig. 7 in main article). Each membrane profile, characterized by its 128 values $(x(t), y(t))$ defines a unique $[\theta_{min}(t)..\theta_{max}(t)]$ range (SI.Fig 2), while flicker noise spectroscopy analysis requires a unique $[\theta_{min}..\theta_{max}]$ range for the angular extension of the whole set of profiles. We define $[\theta_{min}..\theta_{max}]$ so that θ_{min} is the biggest value of the set of $\theta_{min}(t)$, and θ_{max} is the smallest value of the set of $\theta_{max}(t)$, taken over the entire movie, as illustrated in Fig. 7 in main article for the particular case of two profiles only. Please note that the so defined $[\theta_{min}..\theta_{max}]$ range is included in the $[\theta^{AV}_{min}..\theta^{AV}_{max}]$ range of the average, circular shape membrane profile (Fig. 7 in main article).

To summarize, the $(\bar{x}_i, \bar{y}_i)$ sub-pixel coordinates of each membrane profile were first converted into a $r(\theta(t),t)$ profile, and then converted against the $[\theta_0..\theta_{127}]$ unique base of angles common to all images, as already explained above; this last conversion was obtained with a usual spline interpolation. We finally introduce a new variable, h (SI.Fig 2) corresponding to the height between the instantaneous profile and the averaged one:

$$h(\theta,t) = r(\theta,t) - R \qquad (1)$$

In the following we refer to the $h(\theta,t)$ distribution as $h(t)$.

1.2 Spectral analysis

The bending modulus κ and the membrane tension σ are theoretically accessible from the analysis of the spectral distribution of the membrane thermal fluctuations using the theory of Helfrich.[??] Consider a flat, fluctuating membrane of surface area A with small amplitude oscillations relative to its average position, *i.e.* characterized by $h(x,z) \ll \sqrt{A}$, (x,z) being the reference plane of the average membrane. Following Helfrich notation,[?] the energy cost due to both

stretching and bending can be written as:

$$F = \int dA \left[\frac{1}{2}\,\kappa\,(\nabla^2 h)^2 \,+\, \frac{1}{2}\,\sigma\,(\nabla h)^2 \right] \qquad (2)$$

Spatial Fourier transformation gives the energy per q-mode, which is known to be $\frac{1}{2}k_BT$, due to the equipartition theorem. The mean square amplitude of each mode can thus be calculated as:

$$\langle h_q^2 \rangle = \frac{k_BT}{\kappa q^4 \,+\, \sigma q^2} \qquad (3)$$

with $q^2 = q_x^2 + q_z^2$. Though derived for a flat open membrane, this formula can be applied to the modes of a quasi-spherical membrane, given the fact that it might be less valid for the lowest modes.[?]

In the particular case of vesicle observation using video microscopy, measurable membrane fluctuations are in fact that of the circular cut of the equatorial plane of the vesicle around the average membrane position, which is expected to be circular, of radius $\langle R \rangle$. Following the same notations as above, the plane of observation is then the (x,y) plane, and thanks to the cylindrical geometry of the average membrane, $h(x,y)$ profiles can further be expressed into cylindrical coordinates, becoming $h(\theta)$. As a consequence of membrane projection, the dimensionality of the problem is reduced, reading the following mean square amplitude for the membrane fluctuations[?] :

$$\langle h_{q_s}^2 \rangle = L\frac{k_BT}{2\sigma}\left[\frac{1}{q_s} - \frac{1}{\sqrt{\frac{\sigma}{\kappa}+q_s^2}}\right] \qquad (4)$$

with $q_s = \frac{2\pi n}{L}$, and $n \in [0, N/2]$, with $L = 2\pi\langle R \rangle$, and N the number of angles over which the contour is numerized. Note that easy Fast Fourier Transform (FFT) is obtained for N taken as a power of two. As explained in the previous section, membrane profiles $h(t)$ of Movie ESI.M16 (SI.Fig. 1) have been numerized over N =128, regularly spaced values of the angle θ, and their FFT was calculated using available routines in python (https://www.python.org/). q-modes are here calculated for $\langle R \rangle = 9.3$ μm, and $L = \langle R \rangle(\theta_{max} - \theta_{min})$, as explained above. The average spectrum over the whole movie is given in SI.Fig. 3, together with its best fit using expression (4), in function of the wave vector q_s. It can be seen that only the first, low frequency points can be fitted. The corresponding wavevector range is located in the crossover region between the two limiting regimes of the theory, *i.e.* the tension-dominated regime on the lower q_s side, and the bending rigidity-dominated regime, on the higher q_s side. In the first one, the spectrum is described by the limit expression obtained from (4) for $\sigma \gg \kappa q^2$:

$$\lim_{\kappa \to 0} \langle h_{q_s}^2 \rangle \;=\; L\frac{k_BT}{2\sigma}\, q_s^{-1} \qquad (5)$$

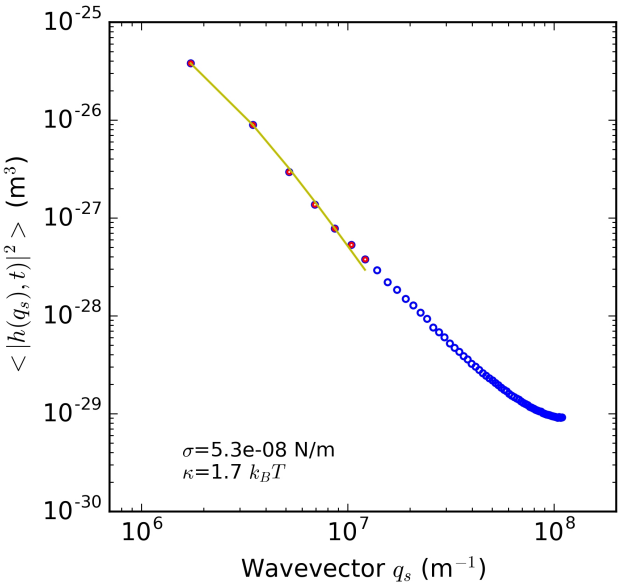

Fig. 3 : Average fluctuation spectrum (○). Best fit (line) is for the first seven wavevectors values (corresponding tension and bending modulus given as inset). Experimental points start deviating from the theoretical fit for *circa* $q_s = 10^7$ m^{-1}.

In the second one, the spectrum can be extracted from the theory for a low enough value of the internal tension of the membrane, *i.e.* for $\sigma \ll \kappa q^2$ in eq(4):

$$\lim_{\sigma \to 0} \langle h_{q_s}^2 \rangle \;=\; L\frac{k_BT}{4\kappa}\, q_s^{-3} \qquad (6)$$

Deviation of the experimental spectrum from the q^{-3} slope at high q_s has been described elsewhere,[?] in the case of video imaging. Due to a finite, non zero value of the aperture time of the shutter of the camera, fluctuations with a lifetime shorter than this integration time are not correctly fitted. Although images were here obtained with a scanning method, due to the confocal technology, leading possibly to subtile, hard to derive effects on the fluctuation spectrum, we can however, as a first estimation, compare our frame acquisition rate of 172 im./sec (i.e. $\tau_{acq} = 5.8$ ms) to the fluctuation lifetime τ_m given by[?] :

$$\tau_m(q)^{-1} = \left(\frac{1}{4q\eta}\right)\,(\sigma q^2 + \kappa q^4) \qquad (7)$$

Under the condition of negligible internal tension on one side, or high internal tension on the other side, we get the corresponding expressions of the wavelength thresholds:

$$q_\kappa^C = \sqrt[3]{\frac{4\eta}{\kappa\tau_{acq}}} \quad \text{and} \quad q_\sigma^C = \frac{4\eta}{\tau\sigma} \qquad (8)$$

with $\eta = 0.001$ kg/m·s the viscosity of the buffer, that reads $q_\kappa^C = 3.5\ 10^6$ m^{-1}, and $q_\sigma^C = 1.3\ 10^7$ m^{-1} respectively, defining a range that includes the wavevector value at which de-

viation between experimental and theoretical spectra starts (SI.Fig. 3).

Clearly our experimental conditions (i.e. mainly reduced observation field and low time resolution) provide partial data as far as spectral analysis is concerned. However, fitting (SI.Fig. 3) reads a value of the membrane bending rigidity $\kappa = 1.7\ k_BT$, *i.e.* in qualitative agreement with that already measured elsewhere.[?]

1.3 Autocorrelation analysis

Autocorrelation analysis

Correlation functions serve as a natural quantity for describing contour fluctuations that are the results of cooperative phenomena within the membrane and its environment. For a given membrane contour, imaged at time t and defined by its distance function $h(\theta,t)$ to the average membrane position (1), we can write the angular correlation function as[?] :

$$A(\theta,t) = \frac{1}{\langle R\rangle^2(\theta_{max}-\theta_{min})}\int_{\theta_{min}}^{\theta_{max}-\theta} h(\phi+\theta,t)\ h(\phi,t)\,d\phi \tag{9}$$

that corresponds here to:

$$A(\theta_n,t) = \frac{1}{128\langle R\rangle^2}\sum_{i=0}^{127-n} h(\theta_i,t)\ h(\theta_{i+n},t) \tag{10}$$

with $\theta_n = \theta_{min} + n\Delta\theta$ since each membrane contour was expressed as a set 128 $h(\theta,t)$ values. While $A(\theta_n,t)$ characterizes a single contour, its time average $\bar{A}(\theta_n)$ is expected to contain general informations about the processes governing membrane shape fluctuations. We thus define the time average over the full sequence of $\mathbf{N} = 1276$ images of Movie ESI.M16 as:

$$\bar{A}(\theta_n) = \frac{1}{\mathbf{N}}\sum_{i=0}^{\mathbf{N}-1} A(\theta_n,t_i) \tag{11}$$

As well explained in previous work,[??] instantaneous membrane undulations around an average, spherical shape, can be expressed by the variable $u(\vartheta,\varphi)$, *i.e.* the distance between the membrane and the average membrane position in the (ϑ,φ), spherical representation:

$$u(\vartheta,\varphi,t) = \sum_{l\geq 0}\sum_{n=-l}^{l} u_{l,n}(t)\ Y_{l,n}(\vartheta,\varphi) \tag{12}$$

with $Y_{l,n}(\vartheta,\varphi)$ the Bessel spherical harmonics, the $u_{l,n}$ corresponding to their amplitudes. Note that previously defined height is $h(\theta,t) = u(\vartheta=\pi/2,\theta)$. In the present case, only the intersection of the membrane with the 2D, focus plane of the objective of the microscope is observed. Thus, the angular autocorrelation function defined above can be expressed as:

$$A(\theta,t) = \sum_{l\geq 0}\sum_{l'\geq 0}\sum_{n\neq 0} u_{l,n}(t)\ u^*_{l',n}(t)\ Y_{l,n}(\frac{\pi}{2},\theta)\ Y^*_{l',n}(\frac{\pi}{2},\theta) \tag{13}$$

Averaging over time enables to simplify (13) by considering that $\langle u_{l,n}(t)\ u^*_{l',n}(t)\rangle = \langle|u_{l,0}|^2\rangle\delta_{ll'}$, thanks to the equipartition theorem.[?] We thus end up with the expression of the average autocorrelation function:

$$\begin{aligned}\bar{A}(\theta) &= \sum_{l\geq 0}\langle|u_{l,0}|^2\rangle\sum_{n=-l}^{l} Y_{l,n}(\frac{\pi}{2},\theta)\ Y^*_{l',n}(\frac{\pi}{2},\theta)\\ &= \sum_{l\geq 0}\langle\xi_l\rangle\ P_l(cos(\theta))\end{aligned} \tag{14}$$

with:

$$\langle\xi_l\rangle = \frac{2l+1}{4\pi}\ \langle|u_{l,0}|^2\rangle \tag{15}$$

and $P_l(x)$ are the Legendre Polynomials. For equilibrium fluctuations of small deviations around the spherical shape, it has been shown that, in absence of a natural curvature of the membrane, the $u_{l,0}$s obey[?] :

$$\langle|u_{l,0}|^2\rangle = \frac{k_BT}{\kappa(l-1)(l+2)[l(l+1)+\frac{\sigma R^2}{\kappa}]} \tag{16}$$

Both bending modulus κ and average membrane internal tension σ can thus be obtained by fitting the experimental average autocorrelation distribution (11) by expression (14), using (15) and (16) (SI.Fig. 4). It is worth noting that $\langle\xi_0\rangle$ and $\langle\xi_1\rangle$ correspond to fluctuations of the radius and center of mass respectively of the round shape membrane.[?] They will thus be excluded from the analysis. Finally, index l in (14) is taken in the range $[3..l_{max}]$, where l_{max} is determined so that expression (14) converges with the right level of precision.

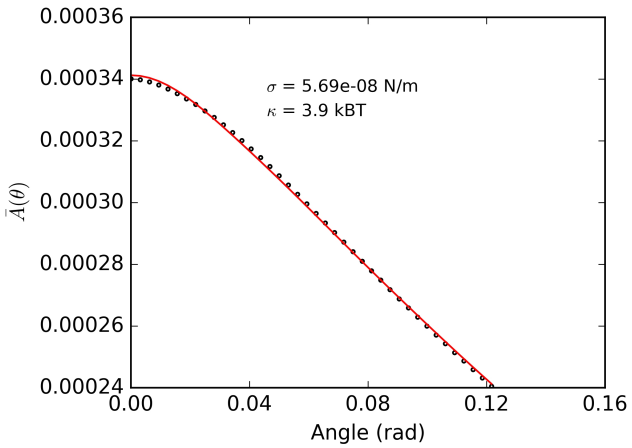

Fig. 4 : Spatial autocorrelation function (○). Best fit (line) reads the tension and bending modulus values given as inset.

The autocorrelation analysis reads a value of the mem-

brane bending rigidity $\kappa = 3.9\ k_BT$ (SI.Fig. 4), closer to that given in litterature[?] than the one obtained with spectrum analysis (see Table 1 in the article).

2 ELECTRONIC SUPPLEMENTARY INFORMATION

Movie M1: LUVs stability at 20°C. Continous movie (3.3 im/s) of a typical $C_{10}E_3$ sample (3.33 g/L) at 20°C. Movie duration corresponds to 96 s; this movie is part of a longer movie (16 min), that shows no evolution of the system all over the period. Image size is 38.75×19.34 μm^2.

Movie M2: Tubes to LUVs transition. Continuous movie (13.8 im/s) of a $C_{10}E_3$ sample T-quenched at 30°C. The sample appears populated by membrane tubes, due to a strong shearing applied during the sample preparation (see Materials and Methods part in the article). Movie duration corresponds to 96 s; this movie is part of a longer movie (217 s). Image size is 38.75×19.34 μm^2. At the end of the sequence are tubes non visible anymore: only LUVs are present, similar to the ones in Movie M1. The whole movie reveals that LUVs remain present up to time 163 s. Only then on do LUVs start to evolve towards multilamellar objects, following the steps described in the article, and finally ending as sponge phase droplets. The observed kinetics of tubes-to-LUVs transition (typically 1.5 min) is way faster than at 20°C, a temperature at which typically 15 to 30 minutes were required.

Movie M3: Bretzel formation. Continuous movie (6.95 im/s) of a $C_{10}E_3$ sample T-quenched at 35°C. The movie shows the typical first stage of LUV structure transformation towards a multilamellar object and later on, eventually towards a sponge phase droplet (not shown). Movie duration corresponds to 14.5 s; this movie is part of Movie M8. Image size is 10.44×9.08 μm^2. Fig. 3 in the article shows six pictures taken from the movie.

Movie M4: T-quentching at 28°C. Continuous movie of a $C_{10}E_3$ sample quenched at 28°C. The movie is build from a time series of xyz-scan intensity averaged projections (38,75×38,75×12,7 μm^3). The movie starts a few seconds after the sample has been introduced in the temperature-controlled environment of the microscope. Total duration corresponds to 6 min 40 s.

Movie M5: T-quentching at 28°C. Continuous movie (13.74 im/s) of a $C_{10}E_3$ sample quenched at 28°C. Image size is 38.75×19.34 μm^2. The movie starts a few seconds after the sample has been introduced in the temperature-controlled environment of the microscope. Movie duration corresponds to 222 s.

Movie M6: T-quentching at 30°C. Movie (1.12 im/s) of a $C_{10}E_3$ sample quenched at 30°C. Movie duration corresponds to 251.2 s. Image size is 38.75×38.75 μm^2. The movie is extracted from a (z,t) scan, *i.e.* the original movie was a continuous sequence of scans over the z-coordinate (over 20.2 μm, 21 steps) over time. The extracted movie corresponds to one z position.

Movie M7: T-quentching at 30°C. Continuous movie of a $C_{10}E_3$ sample quenched at 30°C. The movie is build from a time series of xyz-scan intensity averaged projections (38,75×38,75×12,7 μm^3) recorded immediately after T-quenching. Total duration corresponds to 4 min 9 s.

Movie M8: T-quentching at 35°C. Continuous movie (13.86 im/s) of a $C_{10}E_3$ sample quenched at 35°C. Movie duration corresponds to 32.4 s. Image size is 38.75×19.34 μm^2.

Movie M9: Stable onion-like structures. Continuous movie (25.24 im/s) of a $C_{10}E_3$ sample T-quenched at 28°C, 6 min 20 s after quenching started. Stable multilamellar onions populate the cell. An automatic z-scanning has been imposed, covering a z-range of 20.17 μm (21 steps). Movie duration corresponds to 12.48 s. Image size is 38.75×19.34 μm^2.

Movie M10: Stable, big multilamellar structures. Continuous movie (1.05 im/s) of a $C_{10}E_3$ sample T-quenched at 28°C, 6 min 09 s after quenching started. Stable very large, multilamellar structures could be seen. Movie duration corresponds to 17.2 s. Image size is 91.18×45.54 μm^2.

Movie M11: Zoom on a stable multilamellar structure. Continuous movie (26.4 im/s) of a $C_{10}E_3$ sample T-quenched at 28°C, 14 min 16 s after quenching started. Movie duration corresponds to 24.8 s. Image size is 15.50×7.72 μm^2.

Movie M13: Fusion during T-quenching. Movie (1.12 im/s) of a $C_{10}E_3$ sample T-quenched at 30°C, 3 min 52 s after quenching started. Movie duration corresponds to 149.4 s. Image size is 38.75×38.75 μm^2. The movie is extracted from a (z,t) scan, *i.e.* the original movie was a continuous sequence of scans over the z-coordinate (20.2 μm over 21 steps) over time. The extracted movie corresponds to one z position.

Movie M14: Fusion during T-quenching. Movie (1.14

im/s) of a $C_{10}E_3$ sample T-quenched at 30°C, 5 min 19 s after quenching started. Movie duration corresponds to 37.7 s. Image size is 77.50×77.50 μm^2. The movie is extracted from a (z,t) scan, *i.e.* the original movie was a continuous sequence of scans over the z-coordinate (20.2 μm over 21 steps) over time. The extracted movie corresponds to one z position.

Movie M12: Big, stable intermediate structures at 28°C. Movie (1.16 im/s) of a $C_{10}E_3$ sample T-quenched at 28°C, 9 min 43 s after quenching started. Movie duration corresponds to 21.53 s. Image size is 77.50×77.50 μm^2. The movie is extracted from a (z,t) scan, *i.e.* the original movie was a continuous sequence of scans over the z-coordinate (20.2 μm over 21 steps) over time. The extracted movie corresponds to one z position.

Movie M15: Membrane dome. Continuous movie (27.6 im/s) of a $C_{10}E_3$ sample T-quenched at 28°C, 28 min 14 s after T-quenching started. Movie duration corresponds to 6.95 s. Image size is 19.38×19.38 μm^2.

Movie M16: Isolated bilayer. Continuous movie (172 im/s) of a $C_{10}E_3$ sample quenched at 28°C, 29 min 26 s after T-quenching started. Movie duration corresponds to 7.41 s. Image size is 3.87×1.92 μm^2.